Energy & Environmental Science

ROYAL SOCIETY OF CHEMISTRY

PAPER

View Article Online
View Journal | View Issue

Cite this: *Energy Environ. Sci.*, 2021, **14**, 1506

Promotion of oxygen reduction reaction on a double perovskite electrode by a water-induced surface modification†

Jun Hyuk Kim,‡[a] Seonyoung Yoo,[a] Ryan Murphy,[a] Yu Chen,[a] Yong Ding,[a] Kai Pei,[a] Bote Zhao,[a] Guntae Kim,*[b] YongMan Choi*[c] and Meilin Liu*[a]

Received 23rd June 2020,
Accepted 25th January 2021

DOI: 10.1039/d0ee03283b

rsc.li/ees

Highly efficient air electrodes are a key component of reversible fuel cells for energy storage and conversion; however, the development of efficient electrodes that are stable against water vapor remains a grand challenge. Here we report an air–electrode, composed of double perovskite material $PrBa_{0.8}Ca_{0.2}Co_2O_{5+\delta}$ (PBCC) backbone coated with nanoparticles (NPs) of $BaCoO_{3-\delta}$ (BCO), that exhibits remarkable electrocatalytic activity for oxygen reduction reaction (ORR) while maintaining excellent tolerance to water vapor. When tested in a symmetrical cell exposed to wet air with 3 vol% H_2O at 750 °C, the electrode shows an area specific resistance of ~0.03 Ω cm^2 in an extended period of time. The performance enhancement is attributed mainly to the electrocatalytic activity of the BCO NPs dispersed on the surface of the porous PBCC electrode. Moreover, *in situ* Raman spectroscopy is used to probe reaction intermediates (*e.g.*, oxygen species) on electrode surfaces, as the electrochemical properties of the electrodes are characterized under the same conditions. The direct correlation between surface chemistry and electrochemical behavior of an electrode is vital to gaining insight into the mechanisms of the electrocatalytic processes in fuel cells and electrolysers.

Broader context

Solid oxide fuel cells (SOFCs) represent one of the cleanest options for cost-effective utilization of a wide variety of fuels, from hydrogen to hydrocarbons, coal gas, and renewable fuels. Further, reversible solid oxide cells (rSOCs) are considered an attractive option for co-generation of power and hydrogen, thus ideally suited for large scale energy storage. However, one of the technical hurdles that hinder broad commercialization of these systems is the vulnerability of the state-of-the-art air–electrode materials (*e.g.*, $La_{0.6}Sr_{0.4}Co_{0.2}Fe_{0.8}O_{3-\delta}$ and $La_{0.8}Sr_{0.2}MnO_{3-\delta}$) to water vapor. Accordingly, the development of water–stable air–electrode materials is imperative. In this article, we report our findings in unravelling the mechanism of enhancing the catalytic activity and durability of a new cathode material, $PrBa_{0.8}Ca_{0.2}Co_2O_{5+\delta}$ (PBCC), through a water-mediated surface self-assembly process. In particular, the real-time *in situ* Raman spectroscopic measurement is able to probe molecular species and reaction intermediates on electrode surfaces, providing information vital to gaining insight into the molecular mechanism of water–electrode interactions under fuel cell conditions and to establishing the scientific basis for rational design of advanced water–stable electrodes or catalysts for SOFCs, rSOCs, and other chemical and energy transformation systems.

Introduction

The demand for clean, secure, and sustainable energy technologies is growing rapidly due to the depletion of fossil fuels and due to global warming. In particular, solid oxide fuel cells (SOFCs) have attracted significant attention because they can serve as one of the most efficient and cleanest power sources to convert chemical fuels into electricity.[1,2] SOFCs are well associated with fuel flexibility (*i.e.*, hydrocarbons, coal gas, and renewable fuels).[3,4] Therefore, their inclusion in electricity generation infrastructure can serve as a pragmatic bridge as hydrogen becomes the primary fuel of zero-emission power generation. However, the relatively poor durability of SOFC cathodes poses

[a] *School of Materials Science and Engineering, Georgia Institute of Technology, Atlanta, Georgia 30332, USA. E-mail: meilin.liu@mse.gatech.edu*
[b] *Department of Energy Engineering, Ulsan National Institute of Science and Technology (UNIST), Ulsan, 689-798, Republic of Korea. E-mail: gtkim@unist.ac.kr*
[c] *College of Photonics, National Chiao Tung University, Tainan 71150, Taiwan. E-mail: ymchoi@nctu.edu.tw*

† Electronic supplementary information (ESI) available. See DOI: 10.1039/d0ee03283b

‡ Current address: Department of Materials Science and Engineering, Korea Advanced Institute of Science and Technology, 291 Daehak-ro, Yuseong-gu, Daejeon, 34141, Republic of Korea.

an obstacle hindering their commercial deployment,[5–9] and thus numerous works have been dedicated to cathode design.[10,11] Nonetheless, a dramatic enhancement in the robustness of these cathodes that also allows them to maintain their high catalytic activity toward the electro-reduction of oxygen is required before commercially viable fuel cells can be realized.

One technical challenge facing the development of a high-performance SOFC cathode is to manage the impact of humidity on the oxygen reduction reaction (ORR) outcome.[5–7,12–26] Water vapor is routinely present in ambient air, yet even an infinitesimal amount of water can elicit an immediate increase in the polarization resistance of state-of-the-art $La_{0.6}Sr_{0.4}Co_{0.2}Fe_{0.8}O_{3-\delta}$ (LSCF) and $La_{1-x}Sr_xMnO_{3-\delta}$ (LSM) cathodes.[27–30] It was reported that water incorporation accompanies A-site cation segregation (*e.g.*, Sr^{2+}) in conventional ABO_3-type cathodes, causing irreversible damage,[31–36] although the surface segregation of an electrode does not always have devastating consequences. Indeed, a well-designed exsolution of nanoparticles (NPs) or the exclusion of self-assembled multi-phase/hybrid catalysts has potential as a beneficial strategy to enhance electrode performance.[37–44] In other words, while water has long been considered to be a contaminant in conventional SOFC air-electrodes, the rational design of a highly moisture-tolerant cathode may be plausible as long as water-segregated cations develop to shape catalytically active phases. Thus far, however, no attempt has been made to utilize airborne water to enhance the electrode surface in applications of SOFCs (except for protonic ceramic fuel cells, where water can be a major carrier of protons[45]). Therefore, a novel strategy is essential to accomplish the aforementioned intelligent concept. To this end, parent materials should initially function as a durable backbone, maintaining bulk structural features under humid air. Secondly, water-mediated self-assembled phases on the surface should play an active role in the oxygen electrochemistry. If the aforementioned requirements are met, a genuine solution with which to formulate water-stable electrodes for SOFCs can be realized.

Inspired by this insight, herein we showcase a water-mediated surface self-assembly process that overcomes the problems commonly encountered with humidification of air–electrodes. In this study, we selected layered perovskite $PrBa_{0.8}Ca_{0.2}Co_2O_{5+\delta}$ (PBCC) as the backbone material.[46] PBCC has demonstrated superior electrochemical performance toward the ORR as well as exceptional durability even in atmospheres which contain CO_2 (*e.g.*, degradation rate as low as $\sim 4 \times 10^{-6}$ Ω cm^2 h^{-1} in ambient air containing $\sim$1% CO_2). Our previous study successfully found that when Ba cations are wet-impregnated on the surface of a PBCC electrode, Co ions from the host oxide diffuse out to form a catalytically active nano-phase of $BaCoO_{3-\delta}$ (BCO), which dramatically enhances the ORR kinetics.[47] Considering that H_2O will likely facilitate the segregation of A-site ions, excluded Ba nano-islands will spontaneously become BCO catalysts through a topotactic cation exchange with Co ions (Fig. 1). To the best of our knowledge, this innovative engineering-oriented strategic attempt has not been reported in the literature. The one-step formation of highly active BCO NPs only hinging on water not only benefits the oxygen electro-reduction process but may also open up novel applications to produce functional self-assembled phases on the surfaces of double perovskites. Moreover, we present here direct real-time spectroscopic evidence of oxygen intermediates and their interactions with

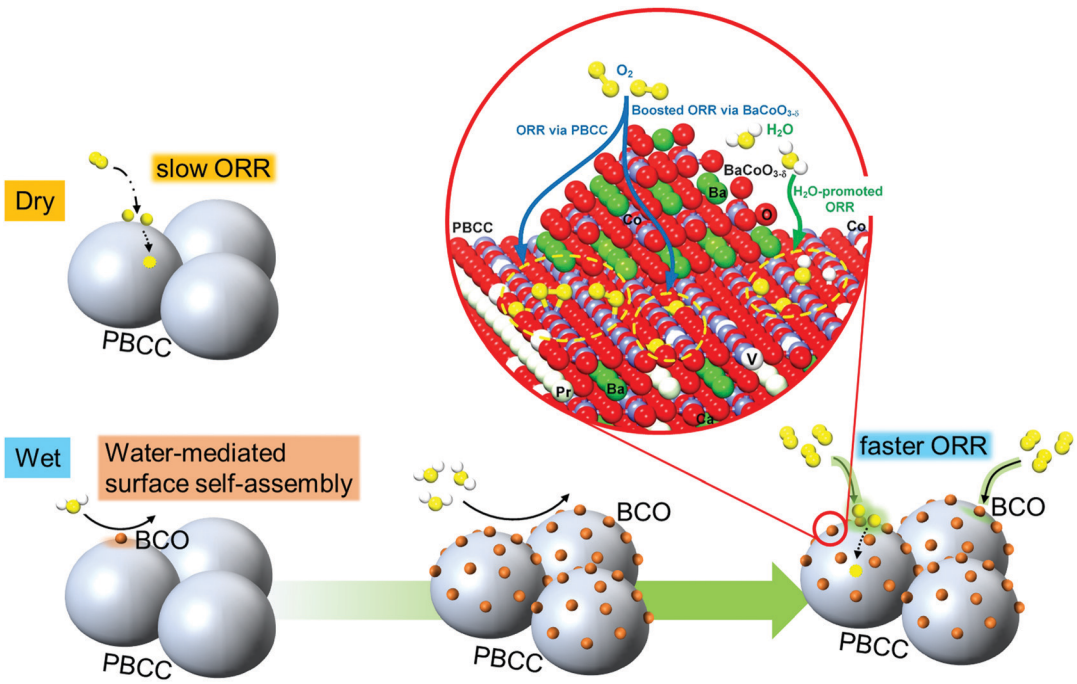

Fig. 1 Schematic illustration of water-mediated surface self-assembly proceeding on double perovskite PBCC.

surface protons with *in situ* Raman spectroscopy as part of the effort to resolve issues related to the complex catalytic processes critical to green energy technologies, such as fuel cells and steam electrolysers.

Results and discussion

Microstructures of water-mediated self-assembled catalyst coatings on PBCC

The backbone material, $PrBa_{0.8}Ca_{0.2}Co_2O_{5+\delta}$ (PBCC), is synthesized with the citric-combustion method. X-ray diffraction (XRD) reveals that PBCC displays the layered perovskite structure of the *P4/mmm* space group, with lattice parameters of $a = b = 3.900$ Å, and $c = 7.618$ Å (Fig. 2a). Shown in Fig. 2b is a high-resolution transmission electron microscopy (HRTEM) image of the as-synthesized PBCC. The length of the unit cell is approximately 0.76 nm, which is consistent with a previous report of the stacking sequence of [Ba(Ca)O]–[CoO_2]–[PrO]–[CoO_2]–[Ba(Ca)O], as clearly shown by the alternating intensities of the line-scan profile in Fig. 2c.[46] The corresponding fast Fourier transform (FFT) pattern exhibiting a superlattice again confirms the double perovskite structure of PBCC (inset in Fig. 2b).

Thereafter, water-mediated surface self-assembly takes place by treating the double perovskites in 3 vol% H_2O/air (hereafter wet air) for 3 h at 600 °C. The temperature of 600 °C is chosen as we previously found out that formation of BCO NPs are confirmed when temperature of ~565 °C is reached.[47] While there is no observable surface decoration on the as-synthesized sample, a scanning electron microscopy (SEM) image (Fig. 2d) and high-angle annular dark-field scanning transmission electron microscopy (HAADF-STEM) (Fig. 2e) of wet-annealed PBCC revealed a multi-phase surface composed of nanoparticles (NPs), as discussed in the introduction. Despite the dramatic change in the surface morphology, PBCC maintained its layered structure (Fig. 2a, top), proving its outstanding chemical compatibility with water. To gain better insight into the composition of the NPs, an energy-dispersive X-ray spectroscopy (EDX) analysis was conducted, as shown in Fig. 2f. EDX confirms that $BaCoO_{3-\delta}$ (BCO) NPs are formed on the bulk PBCC, leading to the production of heterogeneous catalyst-coated surfaces (Fig. S1, ESI†). As noted earlier, the electrocatalytic activity of an electrode can be improved further through the sophisticated control of cation segregation.[37,38,48] The cobalt exsolution on $PrBaCo_2O_{5+\delta}$ (PBC) can be executed by changing the oxygen partial pressure,[49] and cobalt-deficient $PrBaCo_{1.94}O_{5+\delta}$ shows faster surface kinetics compared to the corresponding perfect PBC.[50] Similarly, we previously reported the formation of a multi-phase catalyst coating with BCO NPs

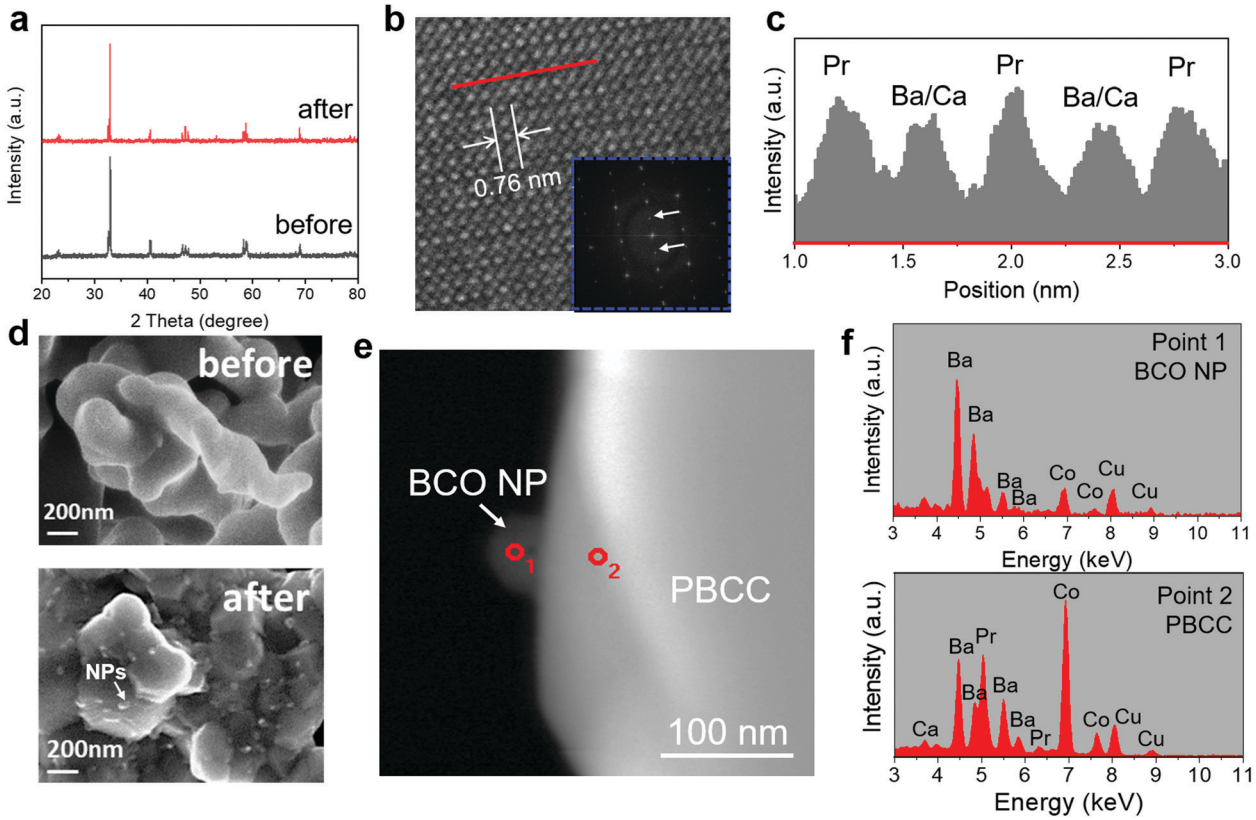

Fig. 2 Microstructures of water-modified PBCC with BCO nano-catalyst coatings: (a) XRD data of the as-synthesized PBCC (gray, bottom) and after 3 vol% H_2O/air exposure at 600 °C for 3 h (red, top). (b) HRTEM image of an as-synthesized PBCC crystal. (inset) FFT pattern showing the superlattice (arrow). (c) Line scan histogram (brightness) along the red line in (b). (d) SEM images of a surface-viewed PBCC electrode before (top) and after (bottom) exposure to 3 vol% H_2O/air at 600 °C for 3 h. After interacting with water, PBCC developed multiple NPs on the surface. (e) HAADF-STEM image of wet-annealed PBCC with a self-assembled BCO NP. (f) EDX analyses of HAADF-STEM at point 1 (O_1, top) and point 2 (O_2, bottom).

on PBCC thin films. BCO NPs significantly enhanced the ORR catalytic activity with a preferentially high O_2 uptake capability.[51]

Raman profilometry was also utilized here to confirm that H_2O mediates such self-assemblies. Raman profilometry is a useful method to analyze proton distributions in dense ceramic pellets.[52,53] In this study, a dense PBCC pellet of 1 mm (Fig. S2, ESI†) is protonated in 3 vol% H_2O/air at 600 °C, and the cross-section of pellet is subsequently analyzed with Raman spectroscopy from the surface to the center (Fig. S3, ESI†). The Raman broad band centered at 3100 cm^{-1} is assigned to OH stretching associated with bulk proton insertion into the PBCC double perovskite.[52,54,55] The distribution of the spectroscopic OH band intensity along the sample depth shows excellent agreement with Fick's second law, which may support the bulk proton diffusion inside of the PBCC double-perovskite structure (Fig. S4, ESI†). We assume that water incorporation into perovskites can hypothetically facilitate dopant segregation in the perovskite structure. Accordingly, this can be the driving force that effectively assembles NPs. As rationally designed, we successfully demonstrated that the BCO NP growth on PBCC is facilitated only by the introduction of water. Raman spectra at a lower vibrational region (100–1200 cm^{-1}) associated with BCO are displayed in Fig. S3b (ESI†). While PBCC shows no observable band due to its cubic symmetry, BCO NPs demonstrate Raman bands similar to the cobaltite phase, presenting bands at 190 cm^{-1} ($F_{2g}^{(3)}$), 490 cm^{-1} (E_g), 520 cm^{-1} ($F_{2g}^{(2)}$), and 690 cm^{-1} (A_{1g}).[47,56] The band distribution of BCO NPs precisely matches that in the OH profiles (Fig. S3a, ESI†), clearly indicating that the NP assembly originates from the introduction of water.

Indeed, water-mediated surface self-assembly is highly effective in tuning the surface morphology of PBCC, in terms of temperature and water vapor pressure. To clearly visualize the morphological change of PBCC, we have controlled the temperature and water partial pressure (pH_2O) as variable, and according sets of SEM analysis is presented on Fig. S5 (ESI†). Initially, the PBCC powder was dry-pressed and corresponding green bodies were sintered at 1120 °C for 10 h to make dense pellets. These pellets are then cleaved and treated with various temperatures and pH_2O to execute water-mediated surface self-assembly. Then the samples are characterized with SEM.

In the dry-annealed samples (Fig. S5a and d, ESI†), the samples show clear surface with no visual sign of nanoparticle formation. However, as water is introduced, the surface of PBCC is decorated with BCO nanoparticles (Fig. S5b, c, e and f, ESI†), as we characterized with TEM previously. Interestingly, we have found out that higher the temperatures and the pH_2O, more effective formation of nanoparticles was identified (Fig. S5g, ESI†).The trend may be the reflection of A-site cation segregation, as it is previously suggested that Sr tends to segregate more in high temperatures and high pH_2O.[34] However, unlike conventional Sr-based cathodes, these segregated particles are developed into catalytically active BCO nanocatalysts. As envisaged, our collective analyses clearly manifest that airborne water modifies the PBCC crystals by liberating Ba and Co ions from the bulk lattice, leading to the *in situ* formation of an active catalyst coating of BCO NPs and ultimately enhancing the ORR kinetics, as described in the next section.

Augmented ORR activity of PBCC electrodes by water introduction

The typical impedance spectra of symmetric cell configurations are measured under open circuit conditions in order to elucidate the electro-catalytic activity of PBCC electrodes for the ORR under humid air (3 vol% H_2O/air) (Fig. 3a top). Notably, changing the oxidant from dry to wet air brings a marked improvement in the size of the impedance arc, implying decreased polarization resistance (R_p) of PBCC. This is attributed to the water-mediated self-assembled catalyst coating, as clearly demonstrated earlier in this paper. The behavior of PBCC is distinctive from that of a state-of-the-art LSCF cathode, which shows sharp degradation under identical experimental conditions (Fig. 3a bottom).

To separate the contributions from each process involved in the ORR, a distribution of relaxation time (DRT) analysis of EIS is performed (Fig. S6 (ESI†), the DRTtools were obtained from Prof. Ciucci's group[57–59]). Indeed, DRT analysis is a powerful technique capable of separating the complex ORR processes in discrete steps according to the relaxation time of different processes, as shown in Fig. S6 (ESI†). The DRT plots for the PBCC sample displayed three distinct peaks: the high-frequency (HF), mid-frequency (MF), and low-frequency (LF) peaks, corresponding to at least 3 elementary steps of the ORR processes. Previously, we have suggested that the process at HF is likely attributed to the charge-transfer across the interface, the one at MF is associated with the oxygen surface exchange (including oxygen dissociation), and the one at LF is related to the mass transfer process such as diffusion.[46,51]

Not surprisingly, after exposure to wet air at 750 °C, the impedances of the processes at MF and LF were dramatically reduced, corresponding to the oxygen surface exchange and diffusion process, respectively. This is consistent with the two-process equivalent circuit model fitting results shown in Fig. S7 and Table S1 (ESI†). To further verify that the rate of the oxygen surface exchange was enhanced, we performed additional electrical conductivity relaxation (ECR) measurement to extract the surface exchange coefficient (k) value (Fig. S8, ESI†). It is found that the k value of PBCC sample annealed in wet air (PBCC wet) is 1.55×10^{-6} cm s^{-1} at 650 °C, which is ~56% higher than that of the pristine PBCC sample (PBCC dry, 9.9×10^{-7} cm s^{-1}). The calculated oxygen-vacancy formation energy for BCO catalyst is 0.55 eV which is much lower than that for PBCC (1.18 eV). Therefore, the rapid oxygen surface exchange of wet-annealed PBCC may be ascribed to the BCO NPs with enriched surface oxygen vacancies, as confirmed by X-ray photoelectron spectroscopy (XPS) analysis (Fig. S9, ESI†). When dissociative oxygen adsorption first takes place at the nano-structured BCO surface, the dissociated oxygen species combine with PBCC at the BCO–PBCC interface *via* fast surface diffusion. As supported by DFT calculations (to be presented later in this manuscript),

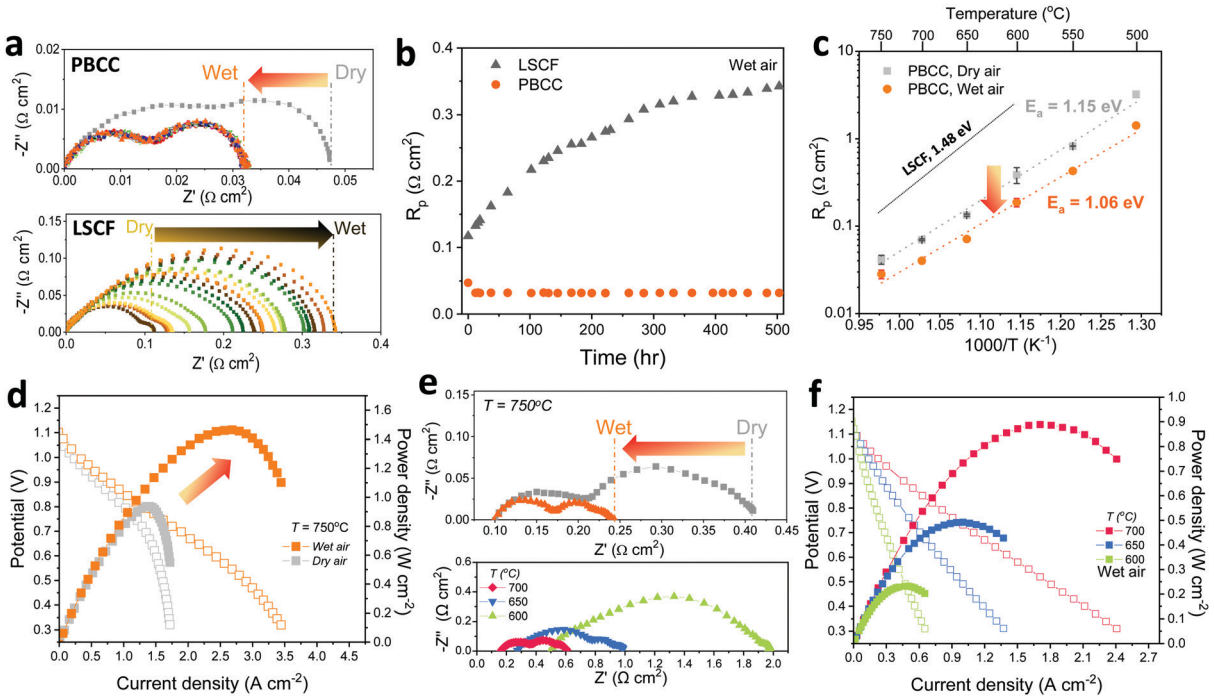

Fig. 3 Electrochemical evaluation of PBCC with water-mediated surface self-assembly (a) electrochemical impedance spectroscopy (EIS) spectra of PBCC (top) and LSCF (bottom) electrodes tested in wet air (3 vol% H_2O/air) at 750 °C. The polarization loss of the PBCC cell decreased dramatically upon the introduction of water. (b) Long-term stability of PBCC electrodes in wet air compared to LSCF electrodes at 750 °C. (c) Arrhenius plot of the polarization resistance of PBCC electrodes in dry/wet air. (d) Comparison of typical *I–V* and *I–P* curves of a button cell with PBCC cathodes in dry/wet air at 750 °C. The Ni–YSZ cell was dwelled under 3 h of wet air to reach equilibrium at 750 °C. (e) Comparison of the impedance spectra of a button cell with PBCC cathodes in dry/wet air at 750 °C (top), and impedance spectra at 600–700 °C under wet air (bottom). Impedance spectra are measured under open circuit voltage. (f) Typical *I–V*, *I–P* curves measured at 600–700 °C.

this step has a lower activation energy in wet atmosphere (0.60 *versus* 1.42 eV). The double perovskite-structured PBCC with self-assembled BCO NPs (catalyst) demonstrates excellent catalytic activity and remarkable tolerance to water vapor. Since the formation of BCO NPs on PBCC can greatly promote the catalytic activity for ORR, it would be highly desirable to develop a wet-chemical process for mass production of BCO–PBCC composite electrodes.

Furthermore, the multi-phase cathode did not show any increase in polarization resistance (R_P) during 500 h of constant exposure to wet air with 3 vol% water vapor (Fig. 3b). Even when exposed to air containing 1 vol% CO_2 and 3 vol% H_2O at 750 °C for an extended duration of more than 325 h (Fig. S10, ESI†), the durable PBCC backbone displayed an exceptional stability in the CO_2 containing atmosphere, while the BCO NPs catalyst derived from the water-mediated self-assembly yields a greatly enhanced electrochemical performance.

A symmetric cell after approximately 200 h of operation in wet air was also examined using SEM and XRD; the results (Fig. S11, ESI†) show exceptional compatibility of the PBCC electrode with the SDC electrolyte and airborne water. The polarization resistances of the PBCC electrodes, with and without the BCO nanoparticle catalysts owing to the airborne water, are also presented in the temperature-dependent Arrhenius plots (Fig. 3c). Indeed, the formation of a multi-phase catalyst changes the oxygen-reduction mechanism because the activation energy (E_a) in humid air (1.06 eV) is much smaller than that in dry air (1.15 eV). It is important to note that PBCC surpasses the performance of LSCF in terms of both the electro-catalytic activity and durability (Fig. S12, ESI†), even under dry air conditions (*i.e.*, no catalyst coating). The water-mediated surface self-assembly can be reproducibly observed with a button cell under realistic SOFC operating conditions. To evaluate its performance, we used an anode-supported cell with a configuration of Ni–yttria stabilized zirconia (Y: 8% mol, YSZ)|scandium stabilized zirconia (Sc: 10% mol, ScSZ). The SDC buffer layer was then deposited between the PBCC electrode and the ScSZ electrolyte to prevent potential side reactions (Fig. S13 (ESI†), cell configuration of Ni–YSZ|ScSZ|SDC|PBCC, Ni–YSZ cell). Subsequently, the resulting button cell was loaded onto a fuel cell testing station and the typical polarization curves were recorded in the temperature range of 600–750 °C (Fig. 3d–f). Dry air was initially fed into the cathode side to investigate the inherent electro-catalytic activity of the PBCC electrode without a catalyst coating (Fig. 3d). Even without the coating, the cell demonstrates a peak power density of approximately 0.94 W cm^{-2} at 750 °C, proving its good electro-catalytic activity. Thereafter, the oxidant was switched from dry to wet air in order to install a BCO catalyst coating mediated by water vapor (Fig. S14, ESI†). The cathode was exposed to wet air for 3 h to achieve water-mediated surface self-assembly. As a result, exceptionally enhanced electrochemical performance is achieved with wet air, as the peak power density

reached approximately 1.46 W cm^{-2} at 750 °C, a nearly 55% increase in the performance compared to that under dry air conditions. To investigate the detailed role of the water-mediated surface self-assembly, electrical impedance spectra are measured under open circuit voltage (Fig. 3e). Similar to the earlier symmetric cell results, the arc resistance improved dramatically from ~0.30 to ~0.14 Ω cm^2. The offset resistance showed no major effects, as it remained ~0.10 Ω cm^2. Given that fuel cells reach their maximal cost-efficiency during operation in ambient air (which naturally contains moisture), the PBCC cathode demonstrated here exhibits intriguing features for a high-performance next-generation oxygen electro-catalyst with exceptional water-contact compatibility. However, as displayed in Fig. S15 (ESI†), excessive water (*e.g.*, >20 vol% H_2O/air) may have a deleterious effect on the electrode performance, suggesting that the water vapor concentration should be carefully tuned for optimal results.

In addition to the Ni–YSZ anode based button cells, we have also applied the multi-phase PBCC cathode to single cells based on a doped ceria electrolyte with Ni–$Sm_{0.2}Ce_{0.8}O_{2-\delta}$ (SDC) or Ni–$Gd_{0.1}Ce_{0.9}O_{2-\delta}$ (GDC10) anodes to examine the potential for applications at lower temperatures (500–650 °C). Both ceria-based single cells were initially heated up to 650 °C to reduce the anode with H_2, while the cathode being exposed to wet air to achieve water-mediated surface self-assembly (detailed procedure and additional experimental results are explained at length in ESI†). Accordingly, superior peak power density of ~0.95 W cm^{-2} can be reached with Ni–SDC|SDC|PBCC single cell (Ni–SDC cell #1, Fig. S16, S17 and Table S2, ESI†) which is nearly two times of the peak power density of the YSZ based single cell at 650 °C. The performance of button cell based on GDC (configuration of Ni–GDC10|$Gd_{0.2}Ce_{0.8}O_{2-\delta}$ (GDC20)|PBCC) achieved ~0.408 W cm^{-2} at 500 °C (Fig. S18, ESI†). These results imply that the multi-phase cathode is very promising for operation at low-temperatures. Compared to the fuel cell performances reported recently, our results are among the best ever reported, highlighting that our new cathodes are highly promising for high-performance SOFCs to be operated in a wide range of temperatures (Table S3, ESI†).

It is of great importance to know if the self-assembled surface created by exposure to water vapor is stable when the condition is switched back to dry air, which is a typical SOFC operating condition. Accordingly, we prepare another single cell (cell #2, Ni–SDC|SDC|PBCC), and tracked the power density at a constant cell voltage of 0.70 V at 565 °C, as the oxidant was switched from dry to wet air containing 3 vol% H_2O (Fig. S19, ESI†). In this case, the single cells performance can be compared at identical operating conditions except the gas environment. In the graph, the electrochemical performance enhancement promoted by water-mediated surface self-assembly can be clearly seen. Then we further tracked the evolution of power density of cell #2, which was initially experienced water-mediated surface self-assembly at 565 °C in wet air. During the test, there was little change in power output as the wet air was switched back to dry air (Fig. S20, ESI†), indicating that the electrode structure remains unchanged in dry air once the BCO NPs are formed (Fig. S21, ESI†).

Additionally, long-term stability of the Ni–GDC cell is measured at 500 °C using wet air as oxidant. During the long-term testing at a constant cell voltage of 0.65 V, there was no sign of degradation in performance over 230 h, indicating good water-compatibility of multi-phase PBCC cathode (Fig. S22, ESI†). After the test, the microstructure of the PBCC was analyzed using SEM. For the single cell, electrolyte was ~12.2 μm thick and the cathode was ~10 μm thick (Fig. S23, ESI†), which retained the microstructural features of water-mediated surface self-assembly even after operation at a constant cell voltage for 230 h continuous exposure to steam (Fig. S23b, ESI†). Indeed, *in situ* grown small NPs (less than 100 nm) are observable throughout the cathode surface (Fig. S24, ESI†), signifying the stability of these NPs under the conditions.

Proton solubility of PBCC

As discussed above, the highly efficient BCO NP formation on PBCC upon the addition of water enhances its ORR kinetics. While remarkable morphological approaches have been applied as a sophisticated interpretation of such kinetic properties of PBCC, it is also of great importance to assess the water uptake characteristics of PBCC for a systematic thermodynamic evaluation.[60,61] To understand the proton solubility of PBCC materials in detail, thermogravimetric analyses (TGA) were conducted (Fig. 4a). First, PBCC powders were calcined at 1100 °C to form a single phase, with this followed by exposure to various water vapor pressures (3, 20, and 30 vol% H_2O) at 600 °C for three hours. XRD analyses were then conducted to exclude any uncertainties regarding the chemical compatibility with water (Fig. S25, ESI†). After wet-annealing, TGA was used to monitor the relative mass change as a function of the temperature. As shown in Fig. 4a, while dry-annealed PBCC shows a linear decrease in the oxygen nonstoichiometry, H_2O-exposed PBCC deviates from the linear behavior, implying the temperature-dependent bulk release of water $\left(2OH_o^{\bullet} \rightarrow H_2O_{(g)} + V_o^{\bullet\bullet} + O_o^{\times}\right)$.[61] As the water vapor pressure was increased, the TGA slope decreased precipitously, implying a higher concentration of absorbed protons. Thereby, the extent of water released from the PBCC was calculated, as shown in Fig. 4b. The corresponding van't Hoff equation can be written as follows:

$$K_w = \frac{\left[OH_o^{\bullet}\right]^2}{pH_2O\left[V_o^{\bullet\bullet}\right]\left[O_o^{\times}\right]} = \exp\left[-\frac{\Delta H}{R}\left(\frac{1}{T}\right) + \frac{\Delta S}{R}\right]$$

By using an oxygen nonstoichiometry value of 5.75 (5 + δ) at 400 °C as a reference,[62] the hydration equilibrium constant (K_w) can be computed as ~0.018 at 600 °C with 3 vol% H_2O, comparable to that of $PrBa_{0.5}Sr_{0.5}Co_{1.5}Fe_{0.5}O_{5+\delta}$ (PBSCF) (K_w = ~0.01 at 600 °C).[60] By using the van't Hoff equation, the hydration enthalpy (ΔH) and entropy (ΔS) at 600 °C were found to be −120.28 kJ mol^{-1} and −171.24 J mol^{-1} K^{-1}, respectively. While a significant amount of protons can be observed in double perovskites, their proton solubility is surprisingly different from that of conventional perovskites such as $La_{0.5}Sr_{0.5}CoO_{3-\delta}$ or LSCF, which show no sign of water dissociation in neither TEM analysis nor TGA outcomes.[61,63] While the detailed

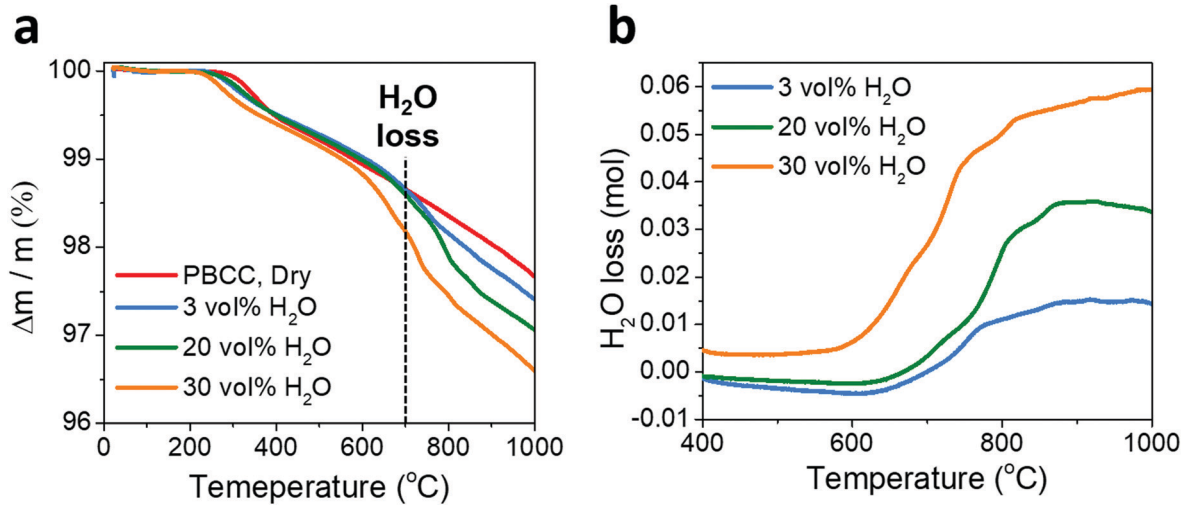

Fig. 4 H_2O uptake behavior of PBCC: (a) thermogravimetric profiles of PBCC powders exposed to different concentrations of water vapor at 600 °C for three hours, and (b) calculated amount of H_2O loss in 1 mol of PBCC.

hydration mechanism should be studied further, it is theorized here that the different crystal structure of double perovskites may be the origin of the more dissolved hydroxyl groups compared to simple perovskites.[60,64] Nevertheless, the presented data are irrefutable evidence of facile water dissociation occurring on PBCC.

Electrochemical oxygen reduction pathways on a protonated double perovskite

The interaction of water with the double perovskite, forming BCO NPs, was discussed in detail above. In this section, we examine closely the surface chemistry of proton and oxygen intermediates. As is well known, for a comprehensive understanding of the ORR kinetics, determining the adsorbed surface species under the given operating conditions and correlating these results with the electrochemical data are essential steps.[46,65] Although computational results for ABO_3-structured perovskites are available in the literature,[66,67] to the best of our knowledge, *in situ* spectroscopic evidence of surface oxygen intermediates on perovskites under SOFC conditions (*i.e.*, at high temperatures) is quite rare. Thus, in this study the ORR mechanism in the presence of surface protons is further elucidated by means of *in situ* time-resolved Raman spectroscopy, which accurately detects surface oxygen species (Fig. 5a, please see Fig. S26 (ESI†) for the detailed experimental setup).[68–70] Information about the surface chemistry as obtained using Raman spectroscopy is then carefully correlated with the electrochemical performance as measured by EIS and density functional theory (DFT) calculations.

The *in situ* spectroscopic evolution of the surface of a PBCC electrode is displayed in Fig. 5b. Since the space group of PBCC belongs to *P*4/*mmm*, it has little Raman activity,[62] and no specific bands appear under dry conditions. On the other hand, switching the gas environment to wet air reveals various surface species, $\nu_1 \sim \nu_4$ (*i.e.*, hydroxyl and oxygen species). These intermediates may indicate that the surface of PBCC is more active in a humidified atmosphere, as their existence was not identified under a dry atmosphere. Because electronically charged oxygen intermediates are reported to be in a broad band regime,[71–74] DFT-based vibrational frequency calculations were applied for an accurate assignment of our measured Raman peaks.

Geometry optimizations using DFT calculations were initially conducted to examine the band assignments and further to determine the discrete steps of the ORR. As shown in Fig. S27 (ESI†), the double-layered perovskite-structure PBCC ($Pr_4Ba_3Ca_1Co_8O_{24}$; *P*4/*mmm*) was prepared. Then, to precisely rationalize the experimental findings using *in situ* Raman spectroscopy, CoO-terminated 8-atomic-layered PBCC(010) surfaces were prepared using a method similar to that in our previous study.[51] Given that the ORR enhancement of BCO NPs was already examined in earlier work by the authors,[51] herein the PBCC surfaces are the major concern. As summarized in Fig. 6a, two types of surface oxygen species (*i.e.*, superoxo and peroxo species) adsorbed at catalytically active Co ion sites ($\mathbf{super_{dry}}$ and $\mathbf{per_{dry}}$, respectively) were initially optimized without hydroxyl species, referring to a dry condition. Their corresponding calculated vibrational frequencies for the O–O stretching mode are 1257 and 917 cm^{-1}, without a scaling factor.

Then, to accurately mimic the water-exposed condition, a hydrogen atom was placed on the surface oxygen ions after verifying the water dissociation on a perfect PBCC(010) surface, which occurs without a barrier (Fig. 6b and Fig. S28, ESI†). This may qualitatively support the excellent water uptake capability of PBCC at high temperatures, as shown in Fig. 4. As illustrated in Fig. S29 (ESI†), the defective surface model has one oxygen vacancy on the surface, resulting in seven active sites for hydrogen adsorption. Using the optimized configurations, we carried out vibrational frequency calculations. Compiled in Tables S4 and S5 (ESI†) are the vibrational frequencies of various oxygen species adsorbed on a defective PBCC surface. Fig. S30 (ESI†) verifies the excellent correlation between the

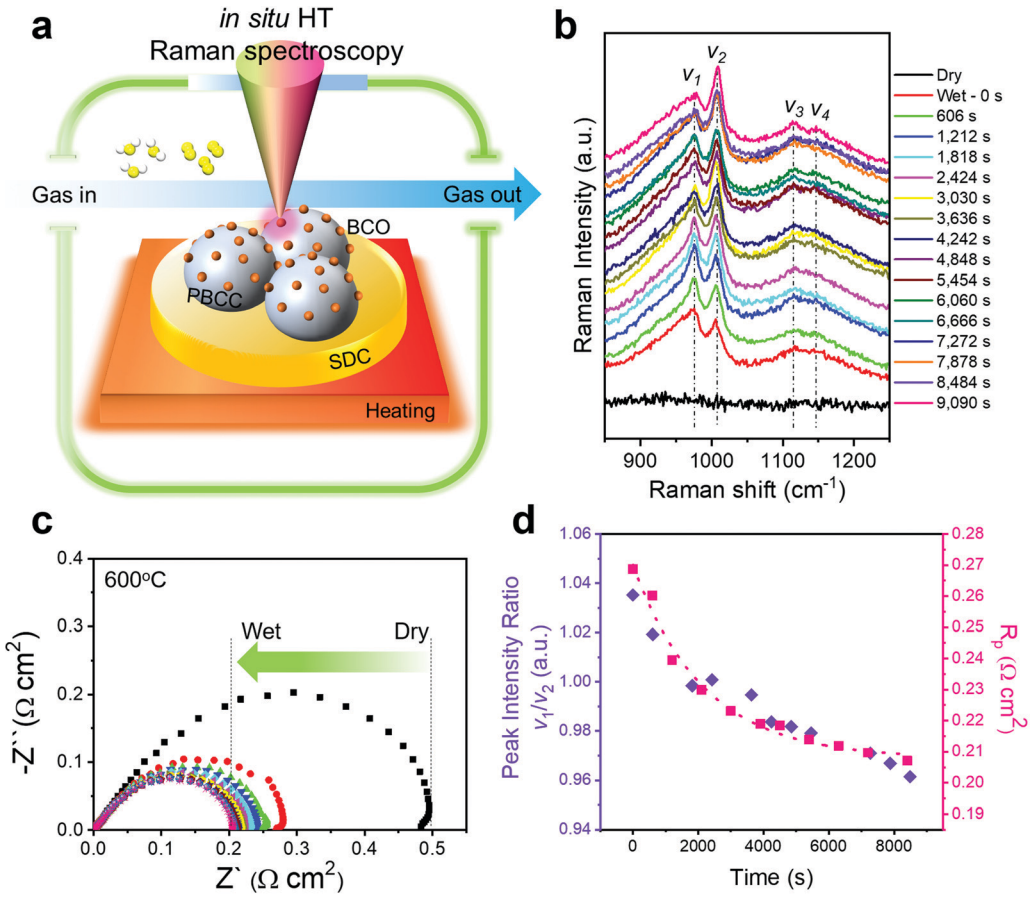

Fig. 5 Unraveling the surface chemistry of PBCC in a humidified atmosphere: (a) schematics of the *in situ* Raman spectroscopy platform with a PBCC|SDC|PBCC symmetric cell. (b) Temporal evolution of the *in situ* Raman spectroscopy of a PBCC surface in a wet air condition (3 vol% H_2O) at 600 °C. Upon exposure to water, various oxygen species are found on the surface, supporting the contention of enhanced ORR activity. (c) Time-resolved EIS spectra of a PBCC symmetric cell in wet air (3 vol% H_2O) at 600 °C. (d) Quantitative correlation between the key features (ν_1/ν_2) of the *in situ* Raman spectrum and the polarization resistance of a PBCC symmetric cell.

vibrational frequencies and the O–O bond lengths as a function of the hydroxyl species. As such, our measured Raman spectral observations of ν_2, ν_3 and ν_4 are a perfect fit to the frequency regime of proton-elongated superoxo species (Table 1).

Indeed, a hydrogen-bond induced redshift of O–O bonds has been reported during water oxidation.[69] However, the observed frequency of ν_1 (977 cm^{-1}) is far from the regime for the peroxo and superoxo region. Thereby, it is more reasonable to assign ν_1 as a bending mode of surface hydroxyl groups, typically observed at ~960 cm^{-1}.[75–77] Overall, the assignment of experimentally observed oxygen species was confirmed with the aid of DFT calculation.

Interestingly, as shown in Fig. 5b, the peak heights of the ν_1 and ν_2 modes at ~977 and ~1006 cm^{-1}, respectively, become reversed after 1800 s. The dynamic change between the two bands, ν_1 and ν_2, implies that they are the primary species in the situation when the water uptake of PBCC equilibrates. Therefore, the relative intensity ratio of the ν_1 and ν_2 modes was calculated and quantitatively synchronized with R_p of an independently measured cell as a function of time (Fig. 5c and d). As shown in Fig. 5d, the peak intensity ratio (ν_1/ν_2) and R_p show an excellent correlation. In particular, as the peak intensity ratio decreases, R_p also decreases, signifying that the hydroxyl and superoxo species actively participate in the major ORR path under wet air.[78]

For a deeper understanding of the highly complex ORR processes, we undertook a mechanistic study using DFT calculations. To propose a plausible mechanism, as schematically depicted in Fig. 6c, we mapped out a minimum-energy profile under dry and wet conditions using the energetics of optimized structures. For the dry pathway, gas-phase oxygen adsorbs at the Co ion on defective PBCC(010) with adsorption energy of −0.86 eV without a barrier (**super$_{dry}$**), after which it becomes more stabilized to a peroxo species due to the incorporation into an oxygen vacancy on the surface without a barrier (**per$_{dry}$**) (−1.12 eV).

On the other hand, the wet pathway was modeled using a PBCC surface with two hydroxyl species (Fig. 6c), which is formed after gas-phase water molecule dissociatively adsorbs as we observed in previous TGA and Raman spectroscopy analysis. The elementary steps from gas-phase oxygen to superoxo species (**super$_{wet}$**, −0.79 eV) was then followed which is consistent with the spectroscopic evidence. After the formation of the peroxo species (**per$_{wet}$**, −1.11 eV), concurrent dissociation and

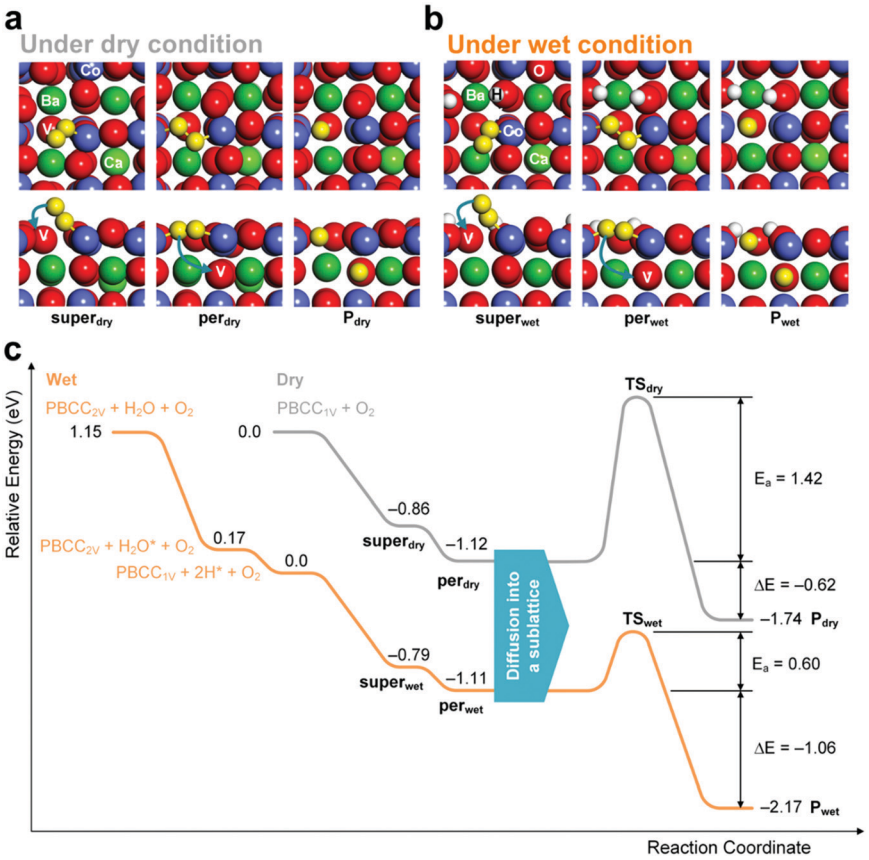

Fig. 6 DFT-based elucidation of the surface chemistry on PBCC: geometrical illustration of typical surface species adsorbed on PBCC(010) used for the mechanistic studies and vibrational frequency calculations (a) under a dry condition and (b) under a wet condition. (c) Schematic of the energy profiles for oxygen reduction on PBCC(010) under dry and wet conditions. E_a and ΔE are correspondingly the reaction barrier height of the concurrent dissociation and diffusion to the sublattice and the reaction energy at 0 K. $PBCC_{1V}$ and $PBCC_{2V}$ denote PBCC with one and two oxygen vacancies, respectively, on the surface.

Table 1 Summary of Raman peaks under wet conditions and their assignments

Mode	Vibrational frequencies (cm^{-1})	Assignment
ν_1	977	Surface hydroxyl
ν_2	1006	Proton-elongated superoxo
ν_3	1114	
ν_4	1148	

diffusion into the sublattice follow, which is the rate-determining step (RDS) in the reaction scheme proposed in this study. Its reaction barrier height under the wet condition is noticeably reduced compared to that under the dry condition (0.60 *versus* 1.42 eV, respectively) which is consistent with the previously shown DRT analysis or the ECR results (Fig. S6 and S8, ESI†).

The correlation between the *in situ* time-dependent Raman measurements and the R_p values determined from impedance spectroscopy could be used for knowledge-based design of efficient SOFC cathode materials by applying molecular-level-based design factors (*i.e.*, a reaction barrier calculation for a RDS in conjunction with a kinetic prediction) and by defining the optimal surface coverage of hydroxyl species, achieving the lowest barrier height under SOFC conditions.

Conclusions

In summary, we have demonstrated a novel approach to achieving nano-structured catalysts on the surfaces of a porous cathode backbone for high ORR activity. A double perovskite PBCC is selected as the cathode because of its high ORR activity and exceptional stability when exposed to water vapor. Indeed, exposure to wet air (with 3 vol% water vapor) results in catalytically active BCO NPs on the surface of PBCC, which dramatically enhance the electrochemical performances (*e.g.*, the peak power density is enhanced from ~0.94 to ~1.46 W cm^2 at 750 °C). In addition, *in situ* Raman spectroscopy is used to probe surface species and reaction intermediates associated with oxygen reduction reaction in wet air. In particular, the spectral evidence for oxygen intermediates on cathode surfaces confirmed in this study is vital to unravelling the mechanism of complex surface electrocatalytic processes under practical conditions. Further, the one-step water-mediated self-assembly process for surface modification of electrodes is applicable to other energy applications, including a solid oxide electrolysis cells and oxygen separation membranes.

Conflicts of interest

There are no conflicts to declare.

Acknowledgements

This work was supported by the US Department of Energy (under award numbers DE-FE0031201 and DE-EE00008439) and US National Science Foundation (under award number DMR-1742828). We are grateful to the National Center for High-performance Computing (NCHC) for computer time and facilities. This work was also supported by the Higher Education Sprout Project of the National Chiao Tung University and Ministry of Education (MOE), Taiwan, and the Mid-Career Researcher Program (NRF-2018R1A2A1A05077532) through the National Reserach Foundation Korea, funded by the Ministry of Science, ICT, and Future Planning.

References

1 Y. Chen, B. deGlee, Y. Tang, Z. Wang, B. Zhao, Y. Wei, L. Zhang, S. Yoo, K. Pei, J. H. Kim, Y. Ding, P. Hu, F. F. Tao and M. Liu, *Nat. Energy*, 2018, **3**, 1042–1050.
2 Z. Gao, L. V. Mogni, E. C. Miller, J. G. Railsback and S. A. Barnett, *Energy Environ. Sci.*, 2016, **9**, 1602–1644.
3 C. Duan, R. J. Kee, H. Zhu, C. Karakaya, Y. Chen, S. Ricote, A. Jarry, E. J. Crumlin, D. Hook, R. Braun, N. P. Sullivan and R. O'Hayre, *Nature*, 2018, **557**, 217–222.
4 E. D. Wachsman and K. T. Lee, *Science*, 2011, **334**, 935–939.
5 C. Pellegrinelli, Y.-L. Huang, J. A. Taillon, L. G. Salamanca-Riba and E. D. Wachsman, *ECS Trans.*, 2014, **64**, 17.
6 B. Hu, M. Keane, M. K. Mahapatra and P. Singh, *J. Power Sources*, 2014, **248**, 196–204.
7 J. S. Hardy, C. A. Coyle, J. F. Bonnett, J. W. Templeton, N. L. Canfield, D. J. Edwards, S. Mahserejian, L. Ge, B. Ingram and J. Stevenson, *J. Mater. Chem. A*, 2018, **6**, 1787–1801.
8 Y. Chen, W. Jung, Z. Cai, J. J. Kim, H. L. Tuller and B. Yildiz, *Energy Environ. Sci.*, 2012, **5**, 7979–7988.
9 P. Hjalmarsson, M. Søgaard and M. Mogensen, *Solid State Ionics*, 2008, **179**, 1422–1426.
10 B. Koo, H. Kwon, Y. Kim, H. G. Seo, J. W. Han and W. Jung, *Energy Environ. Sci.*, 2018, **11**, 71–77.
11 Y. Gong, D. Palacio, X. Song, R. L. Patel, X. Liang, X. Zhao, J. B. Goodenough and K. Huang, *Nano Lett.*, 2013, **13**, 4340–4345.
12 Y. Huang, C. Pellegrinelli and E. Wachsman, *J. Electrochem. Soc.*, 2016, **163**, F171–F182.
13 C. Pellegrinelli, Y.-L. Huang and E. D. Wachsman, *ECS Trans.*, 2019, **91**, 665.
14 B. Hu, M. K. Mahapatra and P. Singh, *J. Ceram. Soc. Jpn.*, 2015, **123**, 199–204.
15 Y.-L. Huang, C. Pellegrinelli and E. D. Wachsman, *ECS Trans.*, 2015, **68**, 699.
16 B. Hu, S. Krishnan, C. Liang, S. J. Heo, A. N. Aphale, R. Ramprasad and P. Singh, *Int. J. Hydrogen Energy*, 2017, **42**, 10208–10216.
17 Y. Chen, Y. Fan, S. Lee, G. Hackett, H. Abernathy, K. Gerdes and X. Song, *J. Power Sources*, 2019, **438**, 227043.
18 A. Hagen, K. Neufeld and Y.-L. Liu, *J. Electrochem. Soc.*, 2010, **157**, B1343.
19 J. Wang, Z. Yang, X. He, Y. Chen, Z. Lei and S. Peng, *Int. J. Hydrogen Energy*, 2019, **44**, 3055–3062.
20 J. Nielsen and M. Mogensen, *Solid State Ionics*, 2011, **189**, 74–81.
21 E. Bucher, W. Sitte, F. Klauser and E. Bertel, *Solid State Ionics*, 2011, **191**, 61–67.
22 E. Bucher, W. Sitte, F. Klauser and E. Bertel, *Solid State Ionics*, 2012, **208**, 43–51.
23 Z. Yang, Y. Liu, Y. Chen, J. Wang, Z. Han, Y. Zhu and M. Han, *Int. J. Hydrogen Energy*, 2017, **42**, 6997–7002.
24 R. Liu, S. Kim, S. Taniguchi, T. Oshima, Y. Shiratori, K. Ito and K. Sasaki, *J. Power Sources*, 2011, **196**, 7090–7096.
25 S. Kim, K. B. Shim, C. Kim, J. Chou, T. Oshima, Y. Shiratori, K. Ito and K. Sasaki, *J. Fuel Cell Sci. Technol.*, 2010, **7**, 021011.
26 Z. Zhao, L. Liu, X. Zhang, W. Wu, B. Tu, D. Cui, D. Ou and M. Cheng, *Int. J. Hydrogen Energy*, 2013, **38**, 15361–15370.
27 J. S. Hardy, J. W. Stevenson, P. Singh, M. K. Mahapatra, E. Wachsman, M. Liu and K. R. Gerdes, *Effects of humidity on solid oxide fuel cell cathodes*, Pacific Northwest National Lab. (PNNL), Richland, WA, 2015.
28 S. D. Ebbesen, C. Graves, A. Hauch, S. H. Jensen and M. Mogensen, *J. Electrochem. Soc.*, 2010, **157**, B1419–B1429.
29 S. Y. Lai, D. Ding, M. Liu, M. Liu and F. M. Alamgir, *ChemSusChem*, 2014, **7**, 3078–3087.
30 S. Benson, D. Waller and J. Kilner, *J. Electrochem. Soc.*, 1999, **146**, 1305–1309.
31 J. Nielsen, A. Hagen and Y.-L. Liu, *Solid State Ionics*, 2010, **181**, 517–524.
32 W. Lee, J. W. Han, Y. Chen, Z. Cai and B. Yildiz, *J. Am. Chem. Soc.*, 2013, **135**, 7909–7925.
33 Z. Cai, M. Kubicek, J. R. Fleig and B. Yildiz, *Chem. Mater.*, 2012, **24**, 1116–1127.
34 B. Koo, K. Kim, J. K. Kim, H. Kwon, J. W. Han and W. Jung, *Joule*, 2018, **2**, 1476–1499.
35 V. Sharma, M. K. Mahapatra, S. Krishnan, Z. Thatcher, B. D. Huey, P. Singh and R. Ramprasad, *J. Mater. Chem. A*, 2016, **4**, 5605–5615.
36 M. Niania, R. Podor, T. B. Britton, C. Li, S. J. Cooper, N. Svetkov, S. Skinner and J. Kilner, *J. Mater. Chem. A*, 2018, **6**, 14120–14135.
37 Y. Li, W. Zhang, Y. Zheng, J. Chen, B. Yu, Y. Chen and M. Liu, *Chem. Soc. Rev.*, 2017, **46**, 6345–6378.
38 D. Neagu, T.-S. Oh, D. N. Miller, H. Ménard, S. M. Bukhari, S. R. Gamble, R. J. Gorte, J. M. Vohs and J. T. Irvine, *Nat. Commun.*, 2015, **6**, 8120.
39 D. Neagu, G. Tsekouras, D. N. Miller, H. Ménard and J. T. Irvine, *Nat. Chem.*, 2013, **5**, 916–923.
40 K. J. Kim, M. K. Rath, H. H. Kwak, H. J. Kim, J. W. Han, S.-T. Hong and K. T. Lee, *ACS Catal.*, 2019, **9**, 1172–1182.
41 Y. Song, Y. Chen, M. Xu, W. Wang, Y. Zhang, G. Yang, R. Ran, W. Zhou and Z. Shao, *Adv. Mater.*, 2020, **32**, 1906979.
42 J. H. Kim, J. K. Kim, H. G. Seo, D. K. Lim, S. J. Jeong, J. Seo, J. Kim and W. Jung, *Adv. Funct. Mater.*, 2020, 2001326.
43 J. Hayd, H. Yokokawa and E. Ivers-Tiffée, *J. Electrochem. Soc.*, 2013, **160**, F351.

44 J. H. Kim, J. K. Kim, J. Liu, A. Curcio, J.-S. Jang, I.-D. Kim, F. Ciucci and W. Jung, *ACS Nano*, 2021, **15**, 81–110.
45 Y. Zhang, A. Zhu, Y. Guo, C. Wang, M. Ni, H. Yu, C. Zhang and Z. Shao, *Appl. Energy*, 2019, **238**, 344–350.
46 Y. Chen, S. Yoo, Y. Choi, J. H. Kim, Y. Ding, K. Pei, R. Murphy, Y. Zhang, B. Zhao, W. Zhang, H. Chen, Y. Chen, W. Yuan, C. Yang and M. Liu, *Energy Environ. Sci.*, 2018, **11**, 2458–2466.
47 Y. Chen, S. Yoo, W. Zhang, J. H. Kim, Y. Zhou, K. Pei, N. Kane, B. Zhao, R. Murphy, Y. Choi and M. Liu, *ACS Catal.*, 2019, 7137–7142, DOI: 10.1021/acscatal.9b01738.
48 S. Joo, O. Kwon, K. Kim, S. Kim, H. Kim, J. Shin, H. Y. Jeong, S. Sengodan, J. W. Han and G. Kim, *Nat. Commun.*, 2019, **10**, 1–9.
49 D. Tsvetkov, I. Ivanov, D. Malyshkin and A. Y. Zuev, *J. Mater. Chem. A*, 2016, **4**, 1962–1969.
50 L. Zhang, S. Li, T. Xia, L. Sun, L. Huo and H. Zhao, *Int. J. Hydrogen Energy*, 2018, **43**, 3761–3775.
51 Y. Chen, Y. Choi, S. Yoo, Y. Ding, R. Yan, K. Pei, C. Qu, L. Zhang, I. Chang and B. Zhao, *Joule*, 2018, **2**(5), 938–949.
52 A. Slodczyk, P. Colomban, S. Willemin, O. Lacroix and B. Sala, *J. Raman Spectrosc.*, 2009, **40**, 513–521.
53 P. Colomban, O. Zaafrani and A. Slodczyk, *Membranes*, 2012, **2**, 493–509.
54 A. Grimaud, J.-M. Bassat, F. Mauvy, P. Simon, A. Canizares, B. Rousseau, M. Marrony and J.-C. Grenier, *Solid State Ionics*, 2011, **191**, 24–31.
55 D. I. Ostrovskii, A. M. Yaremko and I. P. Vorona, *J. Raman Spectrosc.*, 1997, **28**(10), 771–778.
56 B. Rivas-Murias and V. Salgueiriño, *J. Raman Spectrosc.*, 2017, **48**, 837–841.
57 M. Saccoccio, T. H. Wan, C. Chen and F. Ciucci, *Electrochim. Acta*, 2014, **147**, 470–482.
58 T. H. Wan, M. Saccoccio, C. Chen and F. Ciucci, *Electrochim. Acta*, 2015, **184**, 483–499.
59 F. Ciucci and C. Chen, *Electrochim. Acta*, 2015, **167**, 439–454.
60 S. Choi, C. J. Kucharczyk, Y. Liang, X. Zhang, I. Takeuchi, H.-I. Ji and S. M. Haile, *Nat. Energy*, 2018, **3**, 202–210.
61 A. Grimaud, F. Mauvy, J. Bassat, S. Fourcade, L. Rocheron, M. Marrony and J. Grenier, *J. Electrochem. Soc.*, 2012, **159**, B683–B694.
62 C. Lim, A. Jun, H. Jo, K. M. Ok, J. Shin, Y.-W. Ju and G. Kim, *J. Mater. Chem. A*, 2016, **4**, 6479–6486.
63 B. Han, K. A. Stoerzinger, V. Tileli, A. D. Gamalski, E. A. Stach and Y. Shao-Horn, *Nat. Mater.*, 2017, **16**, 121.
64 E. Vøllestad, R. Strandbakke, M. Tarach, D. Catalán-Martínez, M.-L. Fontaine, D. Beeaff, D. R. Clark, J. M. Serra and T. Norby, *Nat. Mater.*, 2019, **18**, 752.
65 J.-C. Dong, X.-G. Zhang, V. Briega-Martos, X. Jin, J. Yang, S. Chen, Z.-L. Yang, D.-Y. Wu, J. M. Feliu, C. T. Williams, Z.-Q. Tian and J.-F. Li, *Nat. Energy*, 2019, **4**, 60–67.
66 Y. Choi, M. e. C. Lin and M. Liu, *Angew. Chem., Int. Ed.*, 2007, **46**, 7214–7219.
67 Z. Wang, R. Peng, W. Zhang, X. Wu, C. Xia and Y. Lu, *J. Mater. Chem. A*, 2013, **1**, 12932–12940.
68 P. M. Radjenovic and L. J. Hardwick, *Faraday Discuss.*, 2018, **206**, 379–392.
69 M. Zhang, M. de Respinis and H. Frei, *Nat. Chem.*, 2014, **6**, 362.
70 J. H. Kim, Z.-Y. Chern, S. Yoo, B. Deglee, J. Wang and M. Liu, *ACS Appl. Mater. Interfaces*, 2019, **12**, 2370–2379.
71 M.-h. Shao, P. Liu and R. R. Adzic, *J. Am. Chem. Soc.*, 2006, **128**, 7408–7409.
72 H. Yu, A. Baricci, J. Roller, Y. Wang, A. Casalegno, W. E. Mustain and R. Maric, *ECS Trans.*, 2015, **69**, 487–496.
73 M. Tsubaki and N.-T. Yu, *Proc. Natl. Acad. Sci. U. S. A.*, 1981, **78**, 3581–3585.
74 J. Cho, R. Sarangi, J. Annaraj, S. Y. Kim, M. Kubo, T. Ogura, E. I. Solomon and W. Nam, *Nat. Chem.*, 2009, **1**, 568.
75 F. Zhang, C. Yuan, X. Lu, L. Zhang, Q. Che and X. Zhang, *J. Power Sources*, 2012, **203**, 250–256.
76 X. Xie, P. Shang, Z. Liu, Y. Lv, Y. Li and W. Shen, *J. Phys. Chem. C*, 2010, **114**, 2116–2123.
77 L. Alrehaily, J. Joseph and J. Wren, *Phys. Chem. Chem. Phys.*, 2015, **17**, 24138–24150.
78 J. Suntivich, H. A. Gasteiger, N. Yabuuchi, H. Nakanishi, J. B. Goodenough and Y. Shao-Horn, *Nat. Chem.*, 2011, **3**, 546–550.

